Article

Analysis of the Performance of Narrow-Bandgap Organic Solar Cells Based on a Diketopyrrolopyrrole Polymer and a Nonfullerene Acceptor

Tom P. A. van der Pol, Junyu Li, Bas T. van Gorkom, Fallon J. M. Colberts, Martijn M. Wienk, and René A. J. Janssen*

Read Online

ACCESS | 📊 Metrics & More | 📖 Article Recommendations | 🆂🅸 Supporting Information

ABSTRACT: The combination of narrow-bandgap diketopyrro-lopyrrole (DPP) polymers and nonfullerene acceptors (NFAs) seems well-matched for solar cells that exclusively absorb in the near infrared but they rarely provide high efficiency. One reason is that processing of the active layer is complicated by the fact that DPP-based polymers are generally only sufficiently soluble in chloroform (CF), while NFAs are preferably processed from halogenated aromatic solvents. By using a ternary solvent system consisting of CF, 1,8-diiodooctane (DIO), and chlorobenzene (CB), the short-circuit current density is increased by 50% in solar cells based on a DPP polymer (PDPP5T) and a NFA (IEICO-4F) compared to the use of CF with DIO only. However, the open-circuit voltage and fill factor are reduced. As a result, the efficiency improves from 3.4 to 4.8% only. The use of CB results in stronger aggregation of IEICO-4F as inferred from two-dimensional grazing-incidence wide-angle X-ray diffraction. Photo- and electroluminescence and mobility measurements indicate that the changes in performance can be ascribed to a more aggregated blend film in which charge generation is increased but nonradiative recombination is enhanced because of reduced hole mobility. Hence, while CB is essential to obtain well-ordered domains of IEICO-4F in blends with PDPP5T, the morphology and resulting hole mobility of PDPP5T domains remain suboptimal. The results identify the challenges in processing organic solar cells based on DPP polymers and NFAs as near-infrared absorbing photoactive layers.
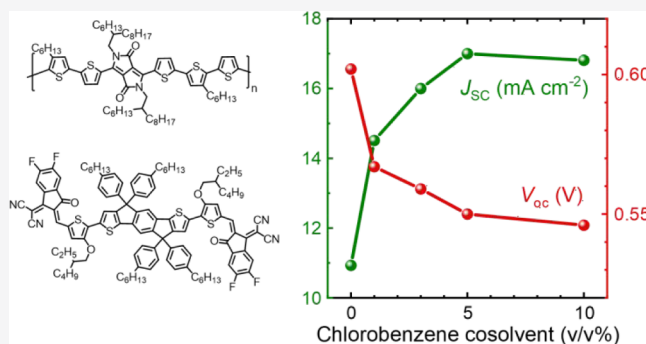
1. INTRODUCTION

In recent years, organic solar cells have been taken by storm by small-molecule nonfullerene acceptors (NFAs).[1−6] NFAs enable record power conversion efficiencies (PCEs) for organic solar cells and provide a rich versatility in optoelectronic properties and processability compared to traditional fullerene acceptors.[7,8] Of specific interest is the fact that the optical absorption of NFAs can extend to the near infrared (NIR).[9,10] To make efficient use of the solar spectrum, NIR-absorbing active layers are crucial, especially for applications in multijunction devices.[11,12] Also, solar cells designed to be transparent to visible light must rely on NIR- and UV-absorbing active layers.[13−15]

For NIR-absorbing active layers, donor−acceptor polymers based on electron-deficient diketopyrrolopyrrole (DPP) units alternating with electron-rich π-conjugated segments are promising candidates because of their narrow optical bandgaps.[16] DPP-based polymers have been successfully incorporated in transistors and in combination with fullerene acceptors in efficient organic single- and multijunction solar cells.[17−23] However, until recently, DPP-polymers mostly gave

moderate PCEs limited to 4.2% when combined with NFAs.[24−26] Two recent examples provide a more promising perspective.[27,28] In the first example, a polymer (PBDTT-DPP) consisting of thiophene-flanked DPP units alternating with alkylthiophene-substituted benzodithiophenes (BDTT) gave a PCE of 9.66% with a NFA.[27] In the second example, a polymer (PffBT-DPP) consisting of a DPP unit, two alkyl-substituted bithiophene units, and a difluorobenzothiadizole (ffBT) in the repeat unit gave a moderate PCE of 2.0% with a NFA in binary blend but up to 9.0% in a ternary blend with a fullerene acceptor.[28] Despite this recent progress, it is currently unclear what causes the efficiency of organic solar cells
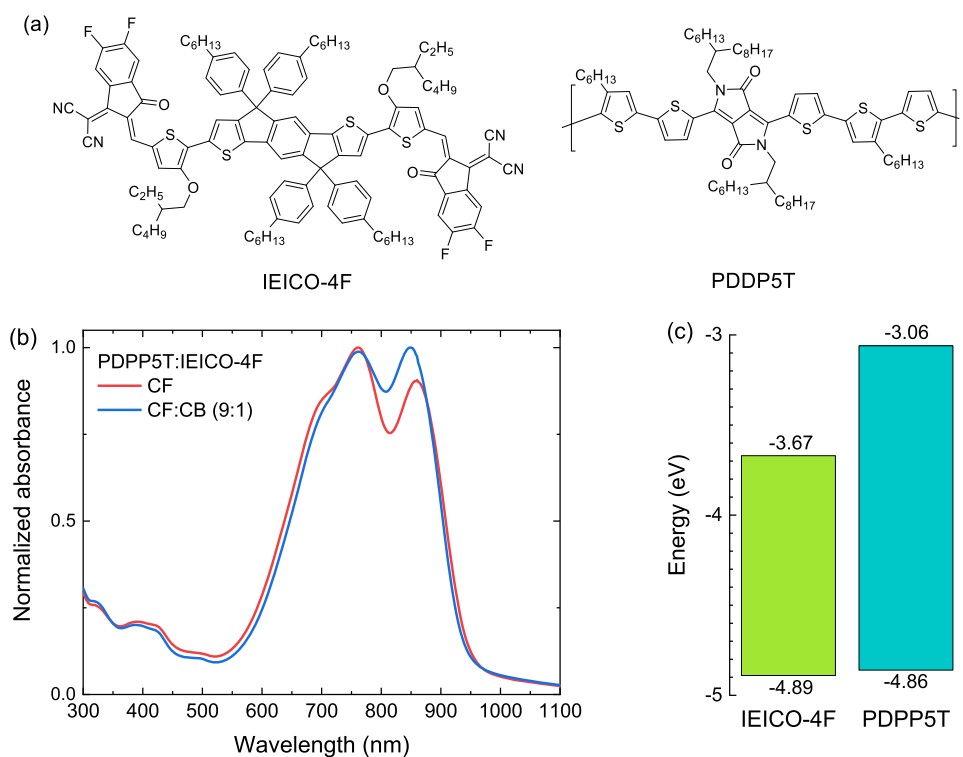
Figure 1. (a) Structures of IEICO-4F and PDDP5T. (b) Normalized absorption spectra of PDPP5T:IEICO-4F (1:2 w/w) blend films cast from CF and CF:CB (9:1 v/v) (c) HOMO and LUMO energies determined *via* SWV.

consisting of DPP-based polymers and NFAs to be moderate in general.

Here, we investigate the efficiency of an organic solar cell based on a blend of PDPP5T and IEICO-4F (Figure 1a) as the active layer using a ternary solvent system. This blend absorbs strongly in the NIR with narrow optical bandgaps for PDPP5T (1.46 eV) and IEICO-4F (1.30 eV). PDPP5T has previously been used with fullerenes in solar cells providing a maximum PCE of 6.5%.[22,23,29,30] As for many DPP polymers, the solubility of PDPP5T in most halogenated and nonhalogenated organic solvents is very limited, but it can be dissolved and conveniently processed from chloroform (CF). So far, the only successful approach to process DPP polymers from nonhalogenated solvents is by creating an asymmetric repeat unit.[31,32] NFAs such as IEICO-4F, on the other hand, are typically processed from chlorobenzene (CB) in which PDPP5T is only sparingly soluble.[27,33−36] This motivated us to investigate a solvent system consisting of mixtures of CF and CB with a small fraction of 1,8-diiodooctane (DIO) as a high-boiling additive. We were interested to understand the effect of CB on the active layer morphology and device performance to understand how DPP-based polymers can be made compatible with NFAs. We conduct this investigation by fabricating and characterizing solar cells, by interpreting interference-corrected photoluminescence (PL) and electroluminescence (EL) spectra, and by investigating the mesoscale morphology. We find that incorporating 3 to 10 vol % CB in the active layer solution increases the short-circuit density (J_{SC}) significantly, coupled to an increase of the maximum external quantum efficiency (EQE) from 34 to 55%, but that this increase is accompanied by a decrease of open-circuit voltage (V_{OC}) and fill factor (FF). We attribute the enhanced EQE to increased crystallinity of IEICO-4F, the loss in V_{OC} to more nonradiative decay, and the lower FF to a decrease in

hole mobility, possibly as a result of a loss of percolation pathways in the polymer phase.

2. EXPERIMENTAL SECTION

2.1. Materials. Patterned tin-doped indium oxide (ITO) covered glass substrates were obtained from Naranjo substrates. Poly(3,4-ethylenedioxythiophene):polystyrene sulfonate (PEDOT:PPS) (Clevios P, VP Al 4083) was purchased from Heraeus. Active layers consist of poly[[2,5-bis(2-hexyldecyl)-2,3,5,6-tetrahydro-3,6-dioxopyrrolo[3,4-*c*]pyrrole-1,4-diyl](3‴,4′-dihexyl-[2,2′:5′,2″:5″,2‴:5‴,2‴′-quinquethiophene]-5,5‴′-diyl)] (PDPP5T)[37] and 2,2′-[[4,4,9,9-tetrakis(4-hexylphenyl)-4,9-dihydro-*s*-indaceno[1,2-*b*:5,6-*b*′]dithiophene-2,7-diyl]bis[[4-[(2-ethylhexyl)oxy]-5,2-thiophenediyl]-methylidyne(5,6-difluoro-3-oxo-1*H*-indene-2,1(3*H*)-diylidene)]]bis[propanedinitrile] (IEICO-4F) (Solarmer Materials). Zinc acetate dihydrate (98+%) (Acros Organics), 2-methoxyethanol (99+%) (Acros Organics), ethanolamine (>99.5%) (Aldrich), MoO₃ (99.99%) (Aldrich), DIO (97+% copper stabilized) (Alfa Aesar), and calcium (99.5%) (Alfa Aesar) were used as received.

2.2. Sample Fabrication. Quartz substrates or Si wafers were cleaned by rinsing with acetone, scrubbing with an isopropanol drenched cloth, rinsing with isopropanol, and finally subjecting to 30 min UV/O₃ treatment prior to deposition. The active layer solution containing 5 mg mL⁻¹ PDPP5T and/or 10 mg mL⁻¹ IEICO-4F was prepared in CF containing 0.2 vol % DIO and a varying concentration of CB. This solution was stirred for 1 h at 80 °C and subsequently allowed to cool to room temperature before further use. The solutions were used to coat cleaned quartz [absorption, PL, and atomic force microscopy (AFM)] or Si-wafer substrates [ellipsometry and two-dimensional grazing-incidence wide-angle X-ray scattering (2D-GIWAXS)], by spin coating for 60 s

at 800 rpm. This gave ~130 nm thick films for the blend. The layers were dried by subjection to high vacuum ($<5 \times 10^{-7}$ mbar) for at least 3 h. Samples for transmission electron microscopy (TEM) were prepared by spin coating the active layer (800 rpm, 60 s) on PEDOT:PSS covered glass substrates, followed by floating the film from the substrate in water and transferring onto a carbon coated 200 square mesh copper grid.

2.3. Solar Cell Fabrication. Inverted configuration ITO/ZnO/active layer/MoO_3/Ag solar cells were prepared by covering cleaned prepatterned ITO substrates with ZnO nanoparticles. These nanoparticles were produced using a sol−gel method where zinc acetate monohydride (109.7 mg) was dissolved in 2-methoxyethanol (1 mL) and ethanolamine (30.2 μL) and stirred for 1 h. The ZnO nanoparticle solution was subsequently spin coated (4000 rpm, 60 s), and the resulting layer was annealed at 150 °C for 5 min to yield ~40 nm thick layers. For regular configuration solar cells (ITO/PEDOT:PSS/active layer/Ca/Ag), a filtered [0.45 μm filter, Pall Life Sciences, Acrodisc, polyvinylidene difluoride membrane] aqueous PEDOT:PSS dispersion was spin coated (3000 rpm, 60 s). Subsequently, the active layer was deposited following the protocol described under sample fabrication. Devices were finalized by thermal evaporation in high vacuum ($<5 \times 10^{-7}$ mbar) of a layer of MoO_3 (10 nm) or Ca (10 nm), for inverted and regular device configurations, respectively, followed by a Ag (100 nm) top contact. Nominal device areas were 0.09 cm^2. Prior to characterization, the inverted configuration solar cells were subjected to UV light (365 nm) from a Spectroline EN-280L/FE lamp for 10 min under a nitrogen atmosphere.

2.4. Characterization. Absorption spectra were recorded on coated quartz substrates using a PerkinElmer Lambda 1050 UV−vis−NIR spectrophotometer.

Square-wave voltammetry (SWV) in 0.1 M tetrabutylammonium hexafluorophosphate ($TBAPF_6$) in ortho-dichlorobenzene (o-DCB) solution (~1.4 mg mL^{-1} IEICO-4F) was performed inside a nitrogen-filled glovebox using a three-electrode setup. A Ag/AgCl reference electrode was freshly prepared, a silver wire was used as the counter electrode, and a platinum electrode was employed as the working electrode. Using an Autolab PGSTAT12 potentiostat, a 0.02 V modulated square-wave voltage with 25 Hz frequency was applied while the voltage was scanned with 0.005 V steps (~0.125 V s^{-1} scan speed). The onsets of the oxidation and reduction waves referenced vs. ferrocene/ferrocenium (Fc/Fc$^+$) as the internal standard were used to determine the highest occupied molecular orbital (HOMO) and lowest unoccupied molecular orbital (LUMO) energies and converted to absolute energies using Fc/Fc$^+$ as −4.59 eV vs vacuum.[38]

A Keithley 2400 SourceMeter was used to measure current density−voltage ($J-V$) characteristics under light and dark conditions. Simulated AM1.5 G conditions were created using a tungsten-halogen lamp with a Schott GG385 UV filter and a Hoya LB120 daylight filter. Measurements were performed in a nitrogen-filled glovebox. The short-circuit current density (J_{SC}) was more accurately determined integrating the EQE spectrum of the cells with the AM1.5 G solar spectrum.

EQE spectra were recorded using a home-built setup, with light from the tungsten-halogen lamp (50 W) mechanically chopped (Stanford Research Systems SR540) and dispersed by a monochromator (Oriel Cornerstone 130) through an aperture (0.0314 cm^2) incident on the cell kept in a nitrogen

atmosphere. The current from the cell was monitored with a low-noise current preamplifier (Stanford Research Systems SR570) and a lock-in amplifier (Stanford Research Systems SR830). A calibrated Si solar cell is used to determine the incident light intensity. Bias light [730 nm light-emitting diode (LED), Thorlabs M730L4] was used in the EQE measurements to create approximate 1-sun illumination conditions by matching the J_{SC} to the value measured with simulated solar light. The use of a tungsten-halogen lamp and the grating monochromator used causes noisy data for wavelengths <360 nm due to low probe light intensities in this region.

To measure EQE in the subbandgap region, an Oriel 3502 light chopper, Cornerstone 260 monochromator (CS260-USB-3-MC-A), a Stanford Research SR 570 preamplifier, a Stanford Research SR830 lock-in amplifier, and a 250 W tungsten-halogen lamp were used. The solar cell was kept in a nitrogen atmosphere during the measurement, and calibrated Si and InGaAs photodiodes were used to determine incident light intensity.

Amplitude and phase difference of the reflected light in the range of 250−1700 nm in air were recorded using a WVASE32 ellipsometer (J.A. Woollam Co.) at angles of 55, 65, and 75°. Optical constants were extracted by fitting a multitude of Gaussian oscillators.

PL spectra were recorded using an Edinburgh Instruments FLSP920 spectrometer, equipped with double monochromators, a xenon arc discharge light-source, and a nitrogen-cooled (−80 °C) NIR sensitive photomultiplier (Hamamatsu R5509-73). The same detector was used to measure EL spectra. Devices were kept in a nitrogen atmosphere during EL experiments.

Nanoscale film AFM topography was performed in tapping mode using a Veeco Dimension 3100 AFM under ambient conditions. A PPP NHCR tip was used (NANOSENSORS).

TEM was performed on a Tecnai G^2 Sphera (FEI) operated at 200 kV.

2D-GIWAXS experiments were carried out using a GANESHA 300 XL+ from JJ X-ray. The system was equipped with a Pilatus 300K detector (172 μm × 172 μm pixel size). The employed X-ray source was a Genix 3D Microfocus sealed tube X-ray Cu-source (1.5408 Å) with an integrated monochromator.

Intensity dependent $J-V$ characteristics were recorded using a Keithley 2400 SourceMeter while illuminating the solar cell with a 730 nm LED (Thorlabs M730L4) through an aperture (0.0314 cm^2) operated at various currents.

Optical simulations were carried out based on the transfer matrix method. An in-house adapted version of the code provided by Burkhard et al.[39] was used to calculate the thickness dependent absorption and the (ultra-low) extinction coefficient. Based on the work of Dyson et al.,[40] Setfos 5.0 (FLUXiM) was employed to calculate the spectral outcoupling efficiency as a function of depth within the active layer for stacks relevant for PL and EL. Then, the outcoupling efficiency was integrated over the relevant depth dependent recombination rate (corresponding to the calculated absorption profile for PL and to unity for EL). This integration yielded wavelength-dependent correction factors which were applied to EL and PL spectra. The correction factor enabled to approximate the intrinsic spectrum of an active layer based on the extrinsic (measured) spectrum. For additional details, we refer to the Supporting Information.
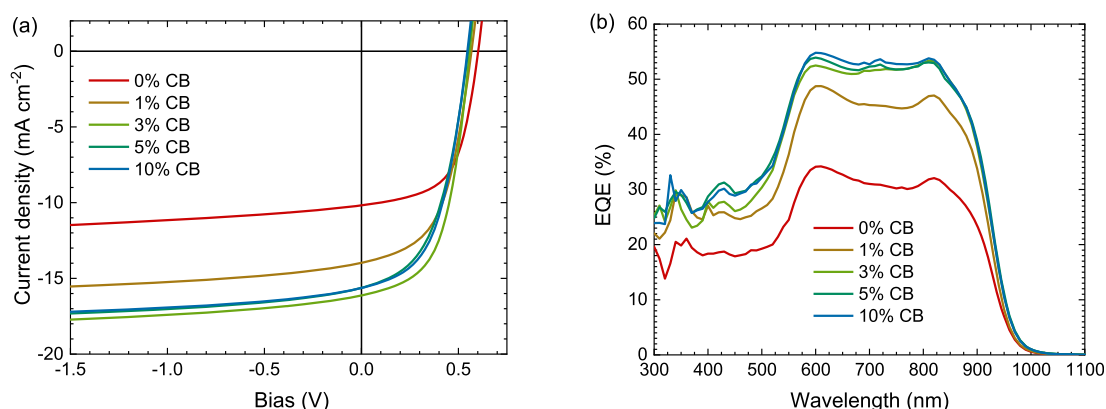
Figure 2. (a) $J-V$ measurements under simulated AM1.5 G (100 mW cm^{-2}) illumination of inverted PDPP5T:IEICO-4F solar cells cast from CF containing 0, 1, 3, 5, or 10 vol % CB and 0.2 vol % DIO. Film thickness is ~130 nm. (b) Corresponding EQE spectra measured with ~1-sun bias illumination.

3. RESULTS AND DISCUSSION

We consider an active layer consisting of a blend of PDPP5T and IEICO-4F in a 1:2 (w/w) ratio. This blend mainly absorbs in the spectral range between 600 to 950 nm (Figure 1b). The absorption coefficients are shown in Figure S1 (Supporting Information). The energies of the HOMO and LUMO of IEICO-4F and PDPP5T (Figure 1c) were determined using SWV. Although all redox potentials are refenced against Fc/Fc$^+$, the conditions were necessarily different. For PDPP5T, SWV was done on a film on a Pt rod immersed in an acetonitrile electrolyte,[38] while for IEICO-4F, SWV was performed in o-DCB solution. The electrochemical bandgaps (E_g^{SWV}) are 1.22 and 1.80 eV for IEICO-4F and PDPP5T, respectively.

PDPP5T:IEICO-4F blend films were used as active layers in inverted glass/ITO/ZnO/active layer/MoO$_3$/Ag solar cells. PDPP5T is typically processed from CF due to its poor solubility in other organic solvents. NFA acceptors such as IEICO-4F often show record efficiencies when cast from CB.[27,33,34] To investigate the consequences of this difference, active layers were spin coated from CF containing 0, 1, 3, 5, or 10 vol % CB and employing 0.2 vol % DIO as a high-boiling additive. DIO was added following an optimized procedure described in the literature.[24] During spin coating, CF will evaporate first because of its higher vapor pressure (21.1 kPa at 20 °C) compared to CB (1.6 kPa at 20 °C). This increases the relative amount of CB and DIO in the drying film with time.[41] Because PDPP5T does not dissolve in CB, it will aggregate at an earlier stage than when using pure CF.[41] This is expected to result in a different extent of phase separation and the high CB content in the final phase of film drying possibly enables more structured IEICO-4F domains. $J-V$ characteristics and EQE spectra for PDPP5T:IEICO-4F cells with 130 nm thick active layers (spin coated at 800 rpm) are shown in Figure 2, and the photovoltaic parameters of best performing devices are summarized in Table 1. Device statistics are available in Table S1 (Supporting Information).

The $J-V$ characteristics show that addition of CB has a strong positive effect on the performance. The J_{SC} and EQE increase by 50%, and a maximum EQE of 55% is among the highest reported for solar cells based on DPP-polymers and NFAs.[24−27,42,43] Figure S2 (Supporting Information) shows a graph of PCEs and maximum EQEs reported in the literature for blends of DPP-polymers with NFAs. The small mismatch

Table 1. Device Characteristics for Best Performing Inverted PDPP5T:IEICO-4F (130 nm) Solar Cells

CB (vol %)	J_{SC} (mA cm^{-2})[a]	J_{SC} (mA cm^{-2})[b]	V_{OC} (V)	FF (-)	PCE (%)[b]
0	10.2	9.7	0.60	0.59	3.4
1	14.0	14.0	0.57	0.53	4.2
3	16.1	15.7	0.56	0.55	4.8
5	15.6	16.1	0.55	0.50	4.4
10	15.6	16.2	0.55	0.52	4.6

[a]J_{SC} from $J-V$ measurements. [b]J_{SC} determined by integrating the EQE spectrum measured with ~1-sun bias illumination.

(2.9 ± 1.8%) between J_{SC} from $J-V$ and from biased EQE experiments stems from imperfect simulation of the solar spectrum by the light source in $J-V$ measurements. The EQE is relatively constant between 600 and 850 nm. The shape of the EQE is related to thin-film cavity effects, giving rise to constructive interference at 600 nm (Figure S3, Supporting Information). The increased EQE must stem from an increase in internal quantum efficiency (IQE) as the absorption changes minimally (Figure S1, Supporting Information). The IQE was calculated for cells cast from CF and CF:CB (9:1) (Figure S3b, Supporting Information) and the average IQE was found to rise from 42 to 64% when 10 vol % CB was included. The increase in J_{SC} when using CB is, however, accompanied by a decrease in V_{OC} and FF. The CB concentration of 3 vol % CB provides a maximal attained PCE of 4.8%. Adding more CB provides virtually identical performance. Also the used D:A ratio was found to have a relatively small effect. Compared to the 1:2 w/w D:A ratio used, 1:1.5 w/w gave similar performance, and only at 1:1 w/w or 1:3 w/w, a loss in performance was noticed (Table S2, Supporting Information). Although moderate on absolute scale, 4.8% is among the higher PCEs reported for DPP-polymer-NFA solar cells (Figure S2, Supporting Information).[26,27,44] Experiments using ~95 nm thick active layers resulted in an increased FF but a lower J_{SC} providing similar PCEs (Figure S4 and Table S3, Supporting Information). The reduced J_{SC} for 95 nm thick films is caused by a reduced EQE at ~600 nm due to a lower fraction of absorbed photons caused by the loss of constructive interference at 600 nm (Figures S3 and S4, Supporting Information). The trends identified for the ~130 nm thick active layers with an increasing amount of CB match those of the ~95 nm thick active layers (Table S3, Supporting
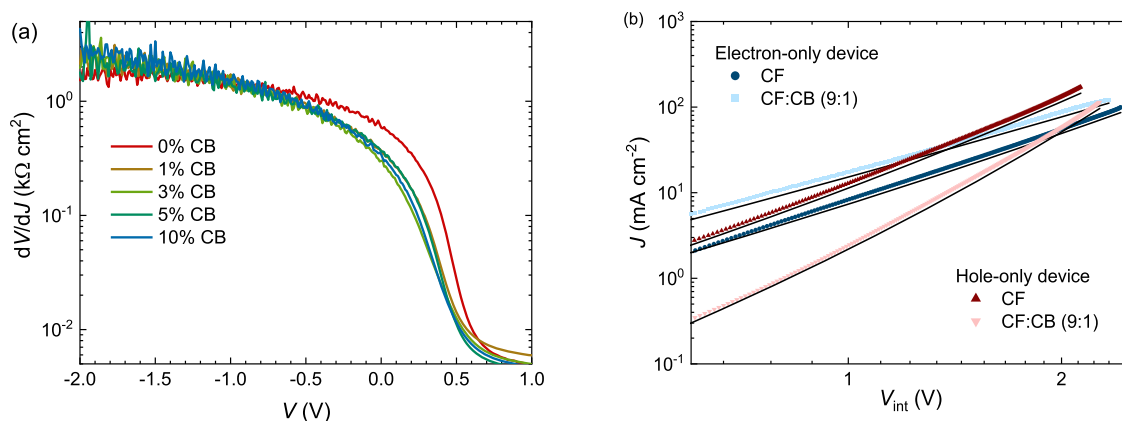
Figure 3. (a) (dV/dJ) as a function of applied bias of the $J-V$ curves shown in Figure 2a. (b) Double logarithmic plot of the $J-V$ characteristics of electron- and hole-only devices with active layers cast from CF and CF:CB (9:1 v/v). Solid lines correspond to fits using the Murgatroyd relation. Layer thickness was 235 ± 5 nm for electron-only and 210 ± 12 nm for hole-only devices.

Information). Increasing the CB concentration further to 15% yielded a small decrease in solar cell performance due to decreasing V_{OC} and FF without a further increase in J_{SC} (Figure S5, Supporting Information). The positive effect induced by using CB was not found when using 1,1,2,2-tetrachloroethane (TCE), which resulted in cells with a PCE of only 0.5% (Figure S6, Supporting Information). TCE has a similar boiling point and vapor pressure (1.9 kPa at 20 °C) as CB, but its solubilizing properties are closer to those of CF (Figure S7, Supporting Information). This illustrates the important role of CB in improving the photovoltaic performance of PDPP5T in blends with IEICO-4F. We have previously shown that high boiling but poor solvents in CF are capable of creating optimal blend morphologies with DPP polymers because they cause the polymer to aggregate before the film is dry and thereby provide improved solar cell performance.[41,45] PDPP5T is much more soluble in TCE than in CB (Figure S7, Supporting Information) which have similar vapor pressures (1.6 kPa for CB vs 1.9 kPa for TCE). Hence, CB and TCE evaporate at the same rate, but CB will cause more aggregation of the polymer before the film is dry. It is likely that other high-boiling poor solvents can have a similar effect as CB.

Figure 2a shows that $J-V$ characteristics under reverse bias have a different magnitude but fairly similar shape for all CB concentrations. This suggests that the low photocurrent found for pure CF is not a consequence of more bimolecular recombination but results from reduced charge generation or more geminate recombination. The inverse derivative of the current density under illumination to the voltage (dV/dJ) as a function of voltage bias (Figure 3a) shows that the apparent shunt resistance [i.e. (dV/dJ) at $V = 0$ V] for cells cast from pure CF is about twice as large as those cast from CF:CB mixed solutions. This implies that in the latter, there is more field-enhanced charge collection because $(dJ/dV)_{V=0}$ is higher.

To test if vertical stratification of PDPP5T and IEICO-4F in the active layer contributes to the reduced FF, regular device configuration cells (glass/ITO/PEDOT:PSS/active layer/Ca/Ag) were fabricated by spin coating the active layer from CF:CB (9:1 v/v). Table S4 and Figure S8 (Supporting Information) show that the performance was not improved and the FF (0.47) was lower than that of the inverted devices.

Table 1 and Figure 2 show that the differences in photovoltaic performance between cells processed with 3, 5, or 10 vol % CB are marginal. This is explained by the

preferential evaporation of CF which causes that in each case, the slower evaporating CB is the predominant solvent in the final stage of film drying where the morphology is established.[41] Because of this effect, the sensitivity to the amount of CB is small above a certain threshold. For PDPP5T:IEICO-4F, this starts at ~3 vol % CB. In subsequent studies, we used 10 vol % CB to investigate the influence of CB and we consider the CF:CB (9:1) layers as a representative for all layers processed with at least 3 vol % CB.

To find the origin of the reduced FF, $J-V$ characteristics of electron-only (ZnO/active layer/Ca/Ag) and hole-only (PEDOT:PSS/active layer/MoO$_3$/Ag) devices in which the active layer was spin coated from CF or from CF:CB (9:1 v/v) were measured. The $J-V$ data (Figure 3b), where the voltage (V_{int}) is corrected for a small built-in potential and the series resistance, show that the electron-only current increases when using CF:CB (9:1 v/v) compared to CF but that the hole-only current decreases. The electron-only current increases quadratically with V_{int} and can be fitted to the Murgatroyd relation $J = (9/8)\varepsilon_0\varepsilon_r\mu_0(V^2/L^3)\exp[0.89\gamma(V/L)^{1/2}]$ for space-charge-limited current with a field-dependent mobility,[46] in which ε_0 is the vacuum permittivity, ε_r the relative permittivity of the active layer (approximated to be 3.5), μ_0 the zero-field mobility, L the thickness of the organic layer, and γ the field-activation factor. Fitting followed the procedure described by Blakesley et al.[47] The results (Figure 3b, Table 2) indicate that

Table 2. Zero-Field Electron Mobility (μ_0) and Field-Activation Factor (γ) in PDPP5T:IEICO-4F Blends Processed from CF:CB Mixtures

CB (vol %)	μ_0 (cm^2 V^{-1} s^{-1})	γ (cm$^{1/2}$ V$^{-1/2}$)
0	$1.5 \pm 0.9 \times 10^{-4}$	$5.8 \pm 1.2 \times 10^{-3}$
10	$4.9 \pm 1.4 \times 10^{-4}$	$1.7 \pm 1.8 \times 10^{-3}$

the electron mobility increases when using CB, and the field-activation factor is lowered. The hole-only current on the other hand decreases when using CB (Figure 3b) and varies with $V_{int}{}^n$, with an exponent $n = 4 - 5$, indicating that it is not space-charge-limited but rather trap-limited. Although these hole-only currents can be fitted to the Murgatroyd relation, unrealistic high field-activation factors are found. The zero-field hole mobility that can be extracted from the fit is more than one order of magnitude lower than for blends of PDPP5T
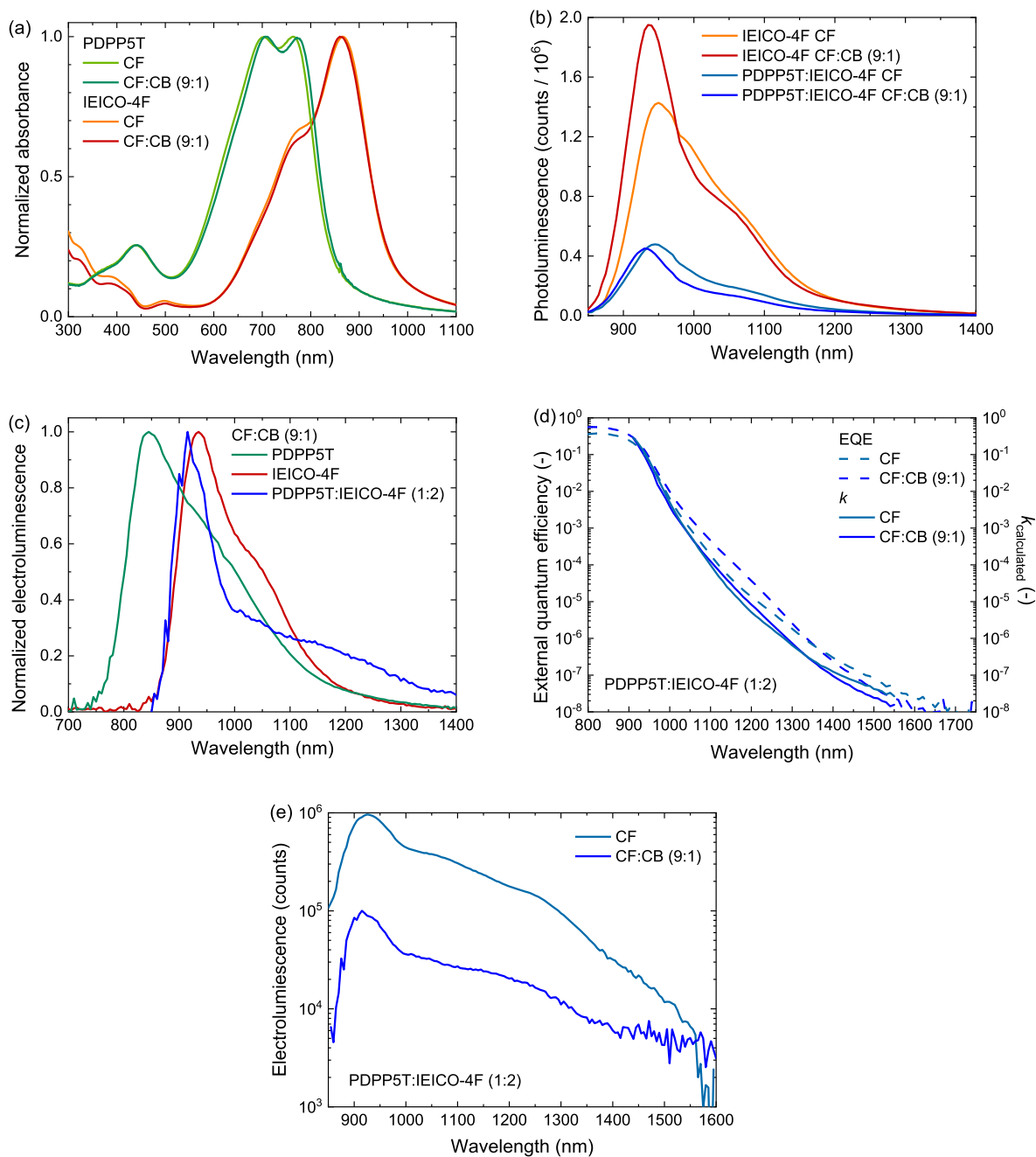
Figure 4. Absorption, PL, EL, and EQE spectra of PDPP5T, IEICO-4F, and PDPP5T:IEICO-4F layers cast from CF and CF:CB (9:1 v/v). All PL and EL spectra were corrected for self-absorption and thin-film interference. (a) Normalized absorption spectra. (b) PL spectra. (c) Normalized EL spectra. (d) Subbandgap region EQE and extinction coefficient (k) calculated for devices employing an active layer of PDPP5T:IEICO-4F. (e) EL spectra of the blend cast from CF and CF:CB (9:1 v/v) measured at 4 V forward bias and current densities of 889 mA cm^{-2} (CF) and 822 mA cm^{-2} [CF:CB (9:1 v/v)].

and [6,6]-phenyl-C_{71}-butyric acid methyl ester ([70]PCBM).[30] It might be that the low offset between the HOMO levels of PDPP5T and IEICO-4F plays a role in reducing the hole mobility. We conclude that the electron mobility increases and the hole mobility decreases when the blends are processed using CF with 10 vol % CB. These trends rationalize the lower FF for blends cast with 10 vol % CB.

Having found an increase in J_{SC} and electron mobility and a concomitant decrease in V_{OC}, FF, and hole mobility when CB is used as a co-solvent, we now aim to elucidate the underlying reasons governing the observed effects. The normalized UV–vis–NIR absorption spectra of PDPP5T and IEICO-4F layers

spin coated from CF without or with 10 vol % CB (Figure 4a) show marginal differences. With 10 vol % CB, the spectrum of PDPP5T slightly redshifts; while for IEICO-4F, the relative peak height of the first vibronic transition (0–0 at 865 nm) increases relative to the intensity of the second vibronic transition (0–1 at 790 nm). These changes indicate a slightly different packing when CB is used.[48,49] The normalized absorption spectra of a blend (1:2 ratio w/w) cast from CF without and with 10 vol % CB (Figure 1b) indicate that the absorption band of IEICO-4F has gained increased intensity relative to the absorption of the PDPP5T upon including CB.

PL spectra of PDPP5T, IEICO-4F, and PDPP5T:IEICO-4F (1:2 w/w) layers cast from CF and CF:CB (9:1 v/v) solutions are shown in Figure S9 (Supporting Information). The spectral line shape of a PL spectrum is influenced by self-absorption and thin-film interference effects originated from the low-finesse cavity formed by the organic layer (See Note S1, Supporting Information).[40] To correct for these effects, we determined the wavelength dependent refractive index ($n(\lambda)$) and extinction coefficient ($k(\lambda)$) of the layers using ellipsometry (Figure S10, Supporting Information), and Figure 4b shows the PL spectra, corrected for self-absorption and optical interference.

Adding CB to CF has a considerable effect on the PL spectra of spin-coated IEICO-4F films (Figure 4b). We attribute the peak at 940 nm to the 0−0 transition and the shoulder at 1040 nm to the 0−1 transition. Upon casting IEICO-4F from a CF:CB (9:1 v/v) solution, the 0−0/0−1 peak ratio increased substantially compared to casting from pure CF, accompanied by an increase in PL intensity. These changes can be ascribed to an enhanced packing of IEICO-4F.[50−53] Figure 4b also shows a small blueshift of the PL spectrum when using CF:CB (9:1 v/v). We interpret this as an indication of less energetic disorder compared to films cast from pure CF.

The PL spectra of the PDPP5T:IEICO-4F blends resemble those of the IEICO-4F. No PL from a CT state can be discerned. The PL of the blend is a factor of 3.0 lower that of IEICO-4F when cast from CF and a factor 4.3 lower when cast from CF:CB (9:1 v/v). The remnant PL indicates incomplete charge generation in these blends, but the increased quenching for CF:CB (9:1 v/v) seems consistent with the increased photocurrent. The use of CB induces a different packing and possibly different phase morphology of IEICO-4F in the blend. Although better intermixing can give rise to more charge-transfer states being formed, better packing in the acceptor phase is commonly linked to enhanced separation of charges from the formed interfacial charge-transfer state and thus lowering geminate recombination and enhancing formation of free charges.[54−58] Furthermore, an improved packing is possibly underlying the observed increase in electron mobility and decrease in field dependence parameter of the electron-only device.

Next, EL spectra were recorded for devices incorporating PDPP5T, IEICO-4F, or PDPP5T:IEICO-4F cast from CF:CB (9:1 v/v) (Figure 4c). Since a solar cell is a low-finesse cavity, these spectra should be corrected for extrinsic contributions to the spectral line shape;[59] the details can be found in the Supporting Information (Note S1 and Figure S11). The corrected EL spectrum of the blend is similar to that of IEICO-4F, indicating that the EL in the solar cell mainly originates from the acceptor phase. Additionally, the EL spectrum of the blend shows a feature at 1250 nm that is not present in the spectra of the pure compounds and which we tentatively attribute to EL from a CT state.[60] At lower bias voltages the contribution of the CT emission at 1250 nm in the EL spectrum increases relative to that of the acceptor phase as shown in normalized EL spectra recorded at 2, 3, and 4 V bias (Figure S12, Supporting Information). This supports the assignment of the 1250 nm emission as stemming from a low energy CT state rather than being a higher vibronic emission band of IEICO-4F.

The presence of this CT state can possibly be discerned in the EQE in the subbandgap region (Figure 4d). This figure also shows the k (extinction coefficient) calculated using the

EQE data in the subbandgap range and a transfer matrix model similar to the protocol described by Kaiser et al.[61] The exact procedure can be found in the Supporting Information (Note S1). Both the EQE and k show an Urbach tail in the subbandgap range and a small (and broad) feature near 1200 nm, possibly originating from absorption of the CT state.

Figure 4e shows the corrected EL spectra for blends cast from CF and from CF:CB (9:1 v/v). The corresponding uncorrected spectra are shown in Figure S13 (Supporting Information). Both EL spectra are dominated by luminescence from IEICO-4F. The spectra show a factor of 10 lower intensity for the blends cast from CF:CB (9:1 v/v) compared to CF. According to the idealized equation[62]

$$\Delta\Delta V_{OC}^{nr} = \Delta V_{OC}^{nr}(1) - \Delta V_{OC}^{nr}(2) = -\frac{k_B T}{q} \ln\left(\frac{EQE_{EL}(1)}{EQE_{EL}(2)}\right)$$

in which ΔV_{OC}^{nr} is the voltage loss due to nonradiative recombination, T the absolute temperature, k_B the Boltzmann constant, q the elementary charge, and EQE_{EL} the external EL quantum efficiency of cells processed without (1) and with (2) CB; the reduction by a factor of 10 in EL intensity results in a V_{OC} loss of about $\Delta\Delta V_{OC}^{nr} = -60$ mV for the cell processed from CF:CB compared to CF only. Further, the radiative limit for the open-circuit voltage (V_{OC}^{rad}) was calculated using idealized equation[62,63]

$$V_{OC}^{rad} = \frac{k_B T}{q} \ln\left(\frac{J_{SC}}{J_{rad}} + 1\right)$$

where

$$J_{SC} = q \int EQE(E)\varphi_{sun}(E)\, dE$$

and

$$J_{rad} = q \int EQE(E)\varphi_{BB}(E)\, dE$$

In these equations, $\varphi_{sun}(E)$ and $\varphi_{BB}(E)$ denote the AM1.5 G spectrum and a black body spectrum at $T = 300$ K as function of energy (E), respectively. The integrals in these equations would ideally span the entire electromagnetic spectrum. We are limited, however, by the noise level when measuring sensitive EQE. Further, Zarrabi et al.[64] have recently shown that using the reciprocity theorem underlying these equations may no longer be valid when considering low-energy states far below the bandgap. We determine V_{OC}^{rad} for different integration limits using the EQEs shown in Figure 4d for the CF and CF:CB (9:1 v/v) cells (Figure S14, Supporting Information). For an integration limit near the noise-level of the EQE measurements ($\sim 2 \times 10^{-8}$), V_{OC}^{rad} is approximately 13 mV higher for the CF:CB (9:1 v/v) blend. The change in open-circuit voltage expected from the EQE and EQE_{EL} is then

$$\Delta V_{OC} = \Delta V_{OC}^{rad} + \Delta\Delta V_{OC}^{nr}$$

and amounts to about −47 mV in good agreement with the −50 mV difference between the two cells measured in the J−V characteristics under simulated AM1.5 G conditions (Table 1).

We investigated the mesoscale morphology of IEICO-4F, PDPP5T, and PDPP5T:IEICO-4F blends cast from CF and from CF:CB (9:1 v/v) using AFM, TEM, and 2D-GIWAXS. In AFM height images, we see a considerable surface roughness for PDPP5T:IEICO-4F blends with small particles at the

surface (Figure 5) (Figure S15, Supporting Information shows the corresponding phase images). This surface roughness is
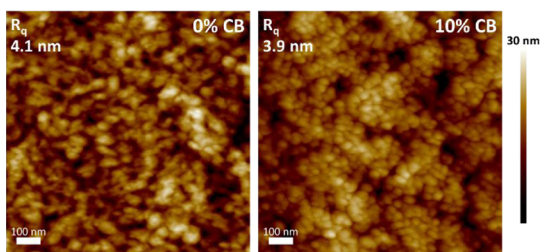

Figure 5. AFM micrographs of PDPP5T:IEICO-4F (1:2 w/w) films cast from CF (left) and CF:CB (9:1 v/v) (right). The root-mean-squared surface roughness is R_q = 4.1 nm (CF) and R_q = 3.9 nm (CF:CB, 9:1 v/v).

attributed to IEICO-4F as it closely resembles the surface of IEICO-4F layers cast from CF (Figures S16 and S17, Supporting Information). The AFM height images show that the addition of 10 vol % CB to the solvent for spin coating results in the formation of more defined particles on the surface compared to pure CF. In TEM, there is little contrast and the observed structures are possibly related to height differences hindering further analysis such as the determination of the domain size (Figure S18, Supporting Information).

To further assess the effect of CB on the morphology of the films, we characterized IEICO-4F, PDPP5T, and PDPP5T:IEI-

CO-4F (1:2 w/w) films by 2D-GIWAXS (Figures S19−S21, Supporting Information). For IEICO-4F, the line cut in the in-plane (IP) direction shows a (100) peak at q_r = 0.31 Å^{-1} (Figure 6a) but without higher-order (h00) reflections indicating an overall low degree of crystallinity. In the out-of-plane (OOP) direction, a (010) peak at q_z = 1.81 Å^{-1} can be seen, corresponding to $\pi-\pi$ stacking (Figure 6b). The results are similar to those reported by Baran et al.[65] Addition of CB results in the appearance of a broad halo at q = 1.5 Å^{-1} for IEICO-4F that is visible in both IP and OOP directions. PDPP5T does not show any clear reflection in the IP or OOP directions when spin coated from CF but develops faint (100) and (010) peaks at q_z = 0.33 Å^{-1} and q_z = 1.64 Å^{-1} in accordance with previous results.[66] The diffraction peaks of the IEICO-4F and PDPP5T are also present in the IP and OOP line cuts of their blend (Figure 6c,d). The intensity increases slightly for the films processed from CF with CB. A hint of long-range order can be seen in the IP direction from the (200) and (300) peaks of IEICO-4F (at q_r = 0.66 and 0.87 Å^{-1}). In the OOP direction for the CF:CB (9:1), the $\pi-\pi$ stacking of IEICO-4F (q_z = 1.83 Å^{-1}) and the (100) peak of PDPP5T (q_z = 0.33 Å^{-1}) are more distinct. Based on these findings, we conclude that spin coating the blend from a CF:CB (9:1 v/v) solvent mixture affects the morphology toward enhanced aggregation of both IEICO-4F and PDPP5T.

Next, we investigated the light intensity dependence of J_{SC}, V_{OC}, and FF using 730 nm excitation (Figure 7a−c) for cells cast from CF and CF:CB (9:1 v/v). The devices show a
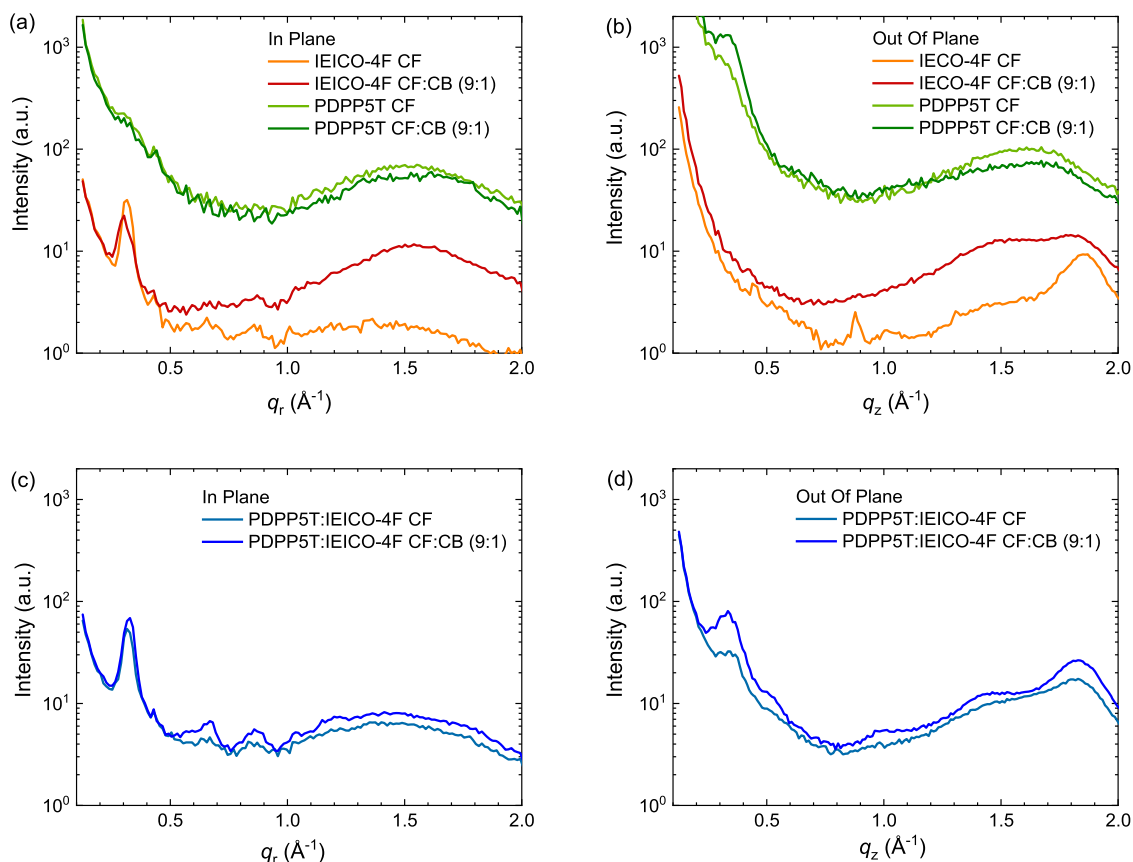

Figure 6. 2D-GIWAXS line cuts from films cast from CF and CF:CB (9:1 v/v). (a) IP for IEICO-4F and PDPP5T. (b) OOP for IEICO-4F and PDPP5T. (c) IP for PDPP5T:IEICO-4F (1:2 w/w). (d) OOP for PDPP5T:IEICO-4F (1:2 w/w). Data for PDPP5T in panels (a,b) are offset vertically for clarity.
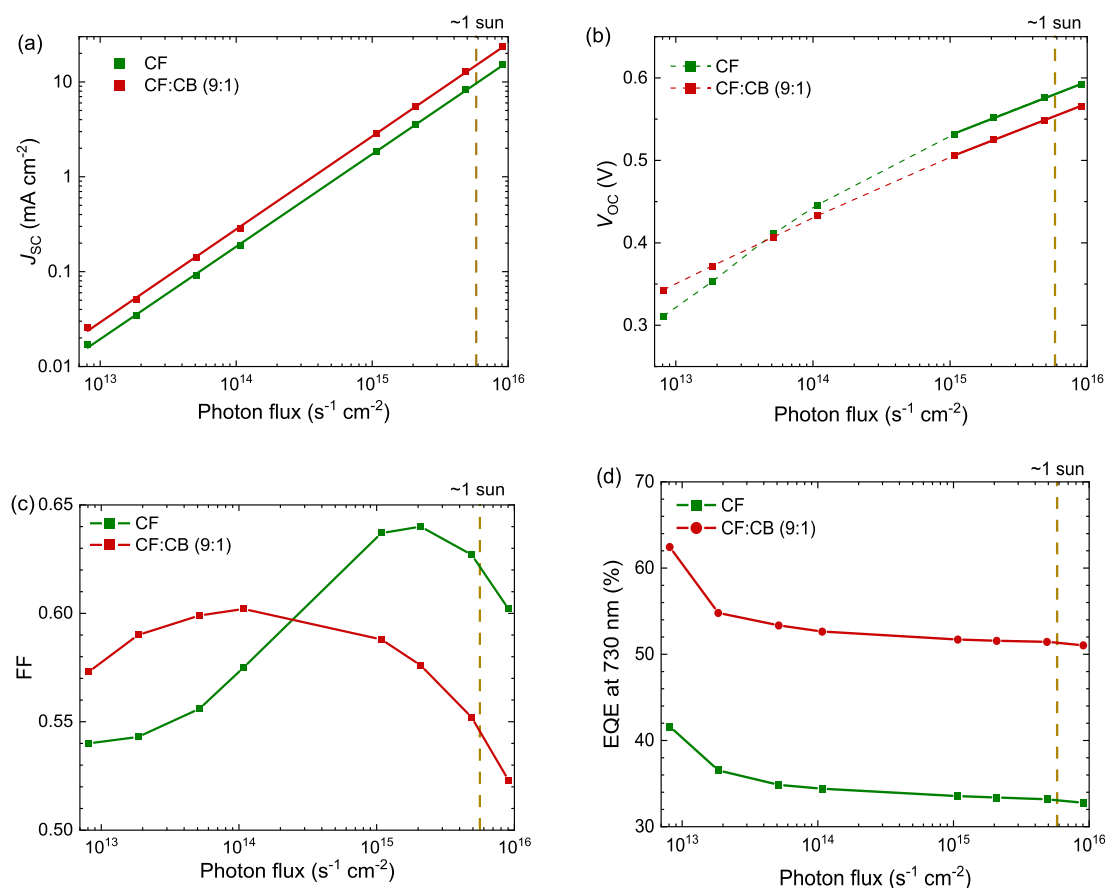
Figure 7. Light intensity dependence of device characteristics of PDPP5T:IEICO-4F solar cells cast from CF and CF:CB (9:1 v/v) solutions. (a) J_{SC}. (b) V_{OC}. (c) FF. (d) EQE at 730 nm.

power-law dependence of J_{SC} on incident light intensity I with exponents of $\alpha = 0.975$ (CF) and $\alpha = 0.980$ (CF:CB (9:1 v/v)). From the light-intensity dependence of V_{OC}, an ideality factor 1.1 is obtained for both cells. Here, we fitted only the higher light-intensity region because at low light intensity, the V_{OC} does not show the expected logarithmic dependence, especially for films cast from pure CF. Such behavior can be due to a small shunt resistance. An ideality factor of 1.1 can be associated with dominant bimolecular recombination or surface recombination. The FF first increases with light intensity but steeply drops toward higher light intensities. For cells processed from CF:CB (9:1 v/v), the drop already starts at a photon flux that corresponds to ~0.02 sun. For cells processed without CB, the decrease in FF sets in at a much higher photon flux (~0.3 sun). A decrease in FF at higher photon fluxes signifies bimolecular charge recombination near the maximum power point. The result that bimolecular recombination is more prone for cells cast from CF:CB (9:1 v/v) than for cells cast from pure CF is consistent with the observed lower shunt resistance when CB is added in the casting solution (Figure 3a) and could be explained by low hole mobility. Figure 7d shows that the light intensity-dependent EQE at 730 nm has a similar shape for both cells, indicating that charge extraction at short-circuit conditions is similar for both devices.

Figure 8 shows the photocurrent defined as the difference between current under illumination and in the dark ($J_{ph} = J_{light} - J_{dark}$) as a function of the effective voltage bias for the devices cast from CF with 0–10 vol % CB. Analogous to the work of
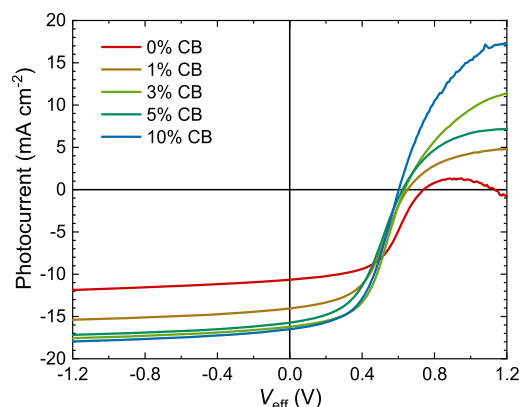

Figure 8. Photocurrent of devices cast from 0, 1, 3, 5, and 10 vol % CB as a function of effective voltage (V_{eff}) over the active layer.

Wehenkel et al.,[67] the effective voltage (V_{eff}) over the active layer was derived from the applied bias (V) by subtracting the voltage drop over the electrodes, using the series resistance ($R_s = 24 \, \Omega$, $\Delta V_{electrodes} = IR_s$). Potential effects of device heating were not regarded. The addition of CB to CF increases the photocurrent under forward bias. Because the forward bias photocurrent can be significantly reduced by charge carriers injected at the contacts, the ratio of photocurrents measured under forward and reverse bias gives information on the extent of Langevin recombination with injected charges.[67] From the photocurrent experiments displayed in Figure 8, it can be

concluded that Langevin recombination with injected charges is suppressed upon CB addition.

In this last section, we rationalize the results from different experiments. PDPP5T:IEICO-4F (1:2 w/w) photovoltaic cells cast from CF:CB (9:1 v/v) give rise to much improved J_{SC} but lower V_{OC} and FF than cells cast from pure CF (Table 1). 2D-GIWAXS experiments show enhanced aggregation of IEICO-4F and PDPP5T when casting layers from CF:CB (9:1 v/v). Enhanced packing of IEICO-4F when using CB also explains the changes in PL spectra and can result in an increased EQE. Larger aggregates and more pure phase domains often give rise to a decrease in V_{OC} because the energy levels of the aggregated phase tend to reduce the bandgap.[68−72] However, a reduction in the optical bandgap is not observed here when comparing the intersection between absorption and PL spectra (Figure S22, Supporting Information). On the other hand, the decrease in EL intensity by about 1 order of magnitude corresponds to a (additional) loss in V_{OC} of ∼60 mV via nonradiative recombination when using CB. Combined with a concomitant slight increase in V_{OC}^{rad} of ∼13 mV, the V_{OC} is expected to decrease by 47 mV in good agreement with the experimental loss (50 mV). At the same time, larger aggregates, enhanced phase separation, and more pure domains commonly result in an increase in FF because these reduce Langevin recombination.[73−77] In contrast, for PDPP5T:IEICO-4F (1:2 w/w) the FF reduces when using CF:CB (9:1 v/v). The reduced FF is not simply related to the lower V_{OC}, rather the absolute difference between V_{OC} and maximum power point voltage (V_{MPP}) increases from 0.142 V for CF to 0.173 ± 0.006 V when adding CB to CF (Figure S23, Supporting Information). Measurements on hole-only devices show that cells processed with CB suffer from a reduced hole mobility. Although PDPP5T shows minimal diffraction peaks in 2D-GIWAXS, the use of CB seems to enhance its aggregation as evidenced by the appearance of a small (100) diffraction peak (Figure 6b,d) and a small redshift of the optical absorption (Figure 4a). Therefore, the lower hole mobility is unlikely due to a reduced packing of PDPP5T chains but possibly due to loss of sufficient percolation pathways. Charges trapped in morphological isolated islands or cul-de-sacs have a higher chance to recombine bimolecularly. Although J_{SC} increases almost linearly with light intensity, the FF for CF:CB (9:1) decreases already at a photon flux larger than ∼0.02 sun (Figure 7c). For cells processed from CF:CB (9:1 v/v), we do not see a reduced photocurrent under forward bias, indicating that recombination with injected charges is small. For solar cell cast from pure CF, recombination with injected charges is stronger.

Currently, we have no fully consistent explanation for the reduced FF when using CB. Evidence of lower bimolecular recombination in forward photocurrent measurements and larger and more crystalline domains of IEICO-4F with higher electron-mobility contrasts somewhat with higher bimolecular recombination in photon flux-dependent FF measurements. Further, the lower hole-mobility remains without evidence of a detrimental morphology in PDPP5T. We hypothesize that the decrease in FF when CB is incorporated in the casting solution stems from this lowered hole mobility and resulting increased bimolecular recombination of photogenerated charges. We speculate that the lowered hole mobility originates from a loss of percolation pathways for holes in the PDPP5T phases of the blend.

4. CONCLUSIONS

Using a ternary solvent mixture consisting of CF, DIO, and CB for casting the active layer, we realized a 50% increase in EQE for PDPP5T:IEICO-4F solar cells compared to a binary solvent mixture of CF and DIO. The increased EQE and J_{SC} resulted in a PCE of 4.8%. Both EQE and PCE are among the highest reported for DPP-based polymers with NFAs. Addition of a few vol % CB to CF containing 0.2 vol % DIO resulted in enhanced stacking of IEICO-4F, which improved charge generation and afforded higher EQEs. The improved J_{SC} is accompanied by a slight decrease in V_{OC}, which is ascribed to more nonradiative decay. Remarkably, also the FF suffers from adding CB. This is a consequence of a decreased hole mobility and increased bimolecular recombination. A fully consistent explanation for the reduced FF cannot be given at this point, but we propose that a loss of percolation pathways in the PDPP5T phase is responsible for the reduced hole mobility and lower FF. This hypothesis is based on the light-intensity dependence of the FF and morphological and spectral characterization. We thus find that CB is essential to obtain well-ordered domains of IEICO-4F in blends with PDPP5T but that the morphology and resulting hole mobility of PDPP5T remain suboptimal. The results described herein clarify some critical processes in processing organic solar cells based on DPP polymers and NFAs as NIR absorbing photoactive layers.

ASSOCIATED CONTENT

Supporting Information

The Supporting Information is available free of charge at https://pubs.acs.org/doi/10.1021/acs.jpcc.0c11377.

> Data on device statistics and on control experiments; optical simulations; IQE data; measured PL and EL spectra; details on the optical simulation method used; and additional AFM, TEM, and GIWAXS data (PDF)

AUTHOR INFORMATION

Corresponding Author

René A. J. Janssen − *Molecular Materials and Nanosystems & Institute for Complex Molecular Systems, Eindhoven University of Technology, Eindhoven 5600 MB, The Netherlands; Dutch Institute for Fundamental Energy Research, Eindhoven 5612 AJ, The Netherlands;* ○ orcid.org/0000-0002-1920-5124; Email: r.a.j.janssen@tue.nl

Authors

Tom P. A. van der Pol − *Molecular Materials and Nanosystems & Institute for Complex Molecular Systems, Eindhoven University of Technology, Eindhoven 5600 MB, The Netherlands*

Junyu Li − *Molecular Materials and Nanosystems & Institute for Complex Molecular Systems, Eindhoven University of Technology, Eindhoven 5600 MB, The Netherlands*

Bas T. van Gorkom − *Molecular Materials and Nanosystems & Institute for Complex Molecular Systems, Eindhoven University of Technology, Eindhoven 5600 MB, The Netherlands*

Fallon J. M. Colberts − *Energy Engineering, Zuyd University of Applied Sciences, Heerlen 6419 DJ, The Netherlands*

Martijn M. Wienk − *Molecular Materials and Nanosystems & Institute for Complex Molecular Systems, Eindhoven*

University of Technology, Eindhoven 5600 MB, The Netherlands

Complete contact information is available at:
https://pubs.acs.org/10.1021/acs.jpcc.0c11377

Notes

The authors declare no competing financial interest.

■ REFERENCES

(1) Zhang, G.; Zhao, J.; Chow, P. C. Y.; Jiang, K.; Zhang, J.; Zhu, Z.; Zhang, J.; Huang, F.; Yan, H. Nonfullerene acceptor molecules for bulk heterojunction organic solar cells. *Chem. Rev.* **2018**, *118*, 3447−3507.

(2) Zhang, J.; Tan, H. S.; Guo, X.; Facchetti, A.; Yan, H. Material insights and challenges for non-fullerene organic solar cells based on small molecular acceptors. *Nat. Energy* **2018**, *3*, 720−731.

(3) Cheng, P.; Li, G.; Zhan, X.; Yang, Y. Next-generation organic photovoltaics based on non-fullerene acceptors. *Nat. Photonics* **2018**, *12*, 131−142.

(4) Ma, R.; Li, G.; Li, D.; Liu, T.; Luo, Z.; Zhang, G.; Zhang, M.; Wang, Z.; Luo, S.; Tao, Y.; et al. Understanding the effect of end group halogenation in tuning miscibility and morphology of high-performance small molecular acceptors. *Sol. RRL* **2020**, *4*, 202000250.

(5) Duan, C.; Ding, L. The new era for organic solar cells: polymer donors. *Sci. Bull.* **2020**, *65*, 1422−1424.

(6) Duan, C.; Ding, L. The new era for organic solar cells: non-fullerene small molecular acceptors. *Sci. Bull.* **2020**, *65*, 1231−1233.

(7) Ma, R.; Liu, T.; Luo, Z.; Guo, Q.; Xiao, Y.; Chen, Y.; Li, X.; Luo, S.; Lu, X.; Zhang, M.; et al. Improving open-circuit voltage by a chlorinated polymer donor endows binary organic solar cells efficiencies over 17%. *Sci. China: Chem.* **2020**, *63*, 325−330.

(8) Ma, R.; Liu, T.; Luo, Z.; Gao, K.; Chen, K.; Zhang, G.; Gao, W.; Xiao, Y.; Lau, T.-K.; Fan, Q.; et al. Adding a third component with reduced miscibility and higher LUMO level enables efficient ternary organic solar cells. *ACS Energy Lett.* **2020**, *5*, 2711−2720.

(9) Cheng, P.; Yang, Y. Narrowing the band gap: The key to high-performance organic photovoltaics. *Acc. Chem. Res.* **2020**, *53*, 1218−1228.

(10) Liu, T.; Ma, R.; Luo, Z.; Guo, Y.; Zhang, G.; Xiao, Y.; Yang, T.; Chen, Y.; Li, G.; Yi, Y.; et al. Concurrent improvement in J_{SC} and V_{OC} in high-efficiency ternary organic solar cells enabled by a red-absorbing small-molecule acceptor with a high LUMO level. *Energy Environ. Sci.* **2020**, *13*, 2115−2123.

(11) Di Carlo Rasi, D.; Janssen, R. A. J. Advances in solution-processed multijunction organic solar cells. *Adv. Mater.* **2019**, *31*, 1806499.

(12) Xie, B.; Chen, Z.; Ying, L.; Huang, F.; Cao, Y. Near-infrared organic photoelectric materials for lightharvesting systems: Organic photovoltaics and organic photodiodes. *InfoMat* **2020**, *2*, 57−91.

(13) Shin, D.; Choi, S.-H. Recent studies of semitransparent solar cells. *Coatings* **2018**, *8*, 329.

(14) Zhang, N.; Chen, G.; Xu, Y.; Xu, X.; Yu, L. Power generation, evaporation mitigation, and thermal insulation of semitransparent polymer solar cells: a potential for floating photovoltaic applications. *ACS Appl. Energy Mater.* **2019**, *2*, 6060−6070.

(15) Romero-Gómez, P.; Pastorelli, F.; Mantilla-Pérez, P.; Mariano, M.; Martínez-Otero, A.; Elias, X.; Betancur, R.; Martorell, J. Semi-transparent polymer solar cells. *J. Photonics Energy* **2015**, *5*, 057212.

(16) Li, W.; Hendriks, K. H.; Wienk, M. M.; Janssen, R. A. J. Diketopyrrolopyrrole polymers for organic solar cells. *Acc. Chem. Res.* **2016**, *49*, 78−85.

(17) Yi, Z.; Sun, X.; Zhao, Y.; Guo, Y.; Chen, X.; Qin, J.; Yu, G.; Liu, Y. Diketopyrrolopyrrole-based π-conjugated copolymer containing β-unsubstituted quintetthiophene unit: A promising material exhibiting high hole-mobility for organic thin-film transistors. *Chem. Mater.* **2012**, *24*, 4350−4356.

(18) Liu, F.; Gu, Y.; Wang, C.; Zhao, W.; Chen, D.; Briseno, A. L.; Russell, T. P. Efficient polymer solar cells based on a low bandgap semi-crystalline DPP polymer-PCBM blends. *Adv. Mater.* **2012**, *24*, 3947−3951.

(19) Dou, L.; You, J.; Yang, J.; Chen, C.-C.; He, Y.; Murase, S.; Moriarty, T.; Emery, K.; Li, G.; Yang, Y. Tandem polymer solar cells featuring a spectrally matched low-bandgap polymer. *Nat. Photonics* **2012**, *6*, 180−185.

(20) Holliday, S.; Li, Y.; Luscombe, C. K. Recent advances in high performance donor-acceptor polymers for organic photovoltaics. *Prog. Polym. Sci.* **2017**, *70*, 34−51.

(21) Di Carlo Rasi, D.; Hendriks, K. H.; Wienk, M. M.; Janssen, R. A. J. Accurate characterization of triple-junction polymer solar cells. *Adv. Energy Mater.* **2017**, *7*, 1701664.

(22) Gevaerts, V. S.; Furlan, A.; Wienk, M. M.; Turbiez, M.; Janssen, R. A. J. Solution processed polymer tandem solar cell using efficient small and wide bandgap polymer:fullerene blends. *Adv. Mater.* **2012**, *24*, 2130−2134.

(23) Kouijzer, S.; Esiner, S.; Frijters, C. H.; Turbiez, M.; Wienk, M. M.; Janssen, R. A. J. Efficient inverted tandem polymer solar cells with a solution-processed recombination layer. *Adv. Energy Mater.* **2012**, *2*, 945−949.

(24) Jung, J. W.; Jo, W. H. A low band-gap copolymer composed of thienyl substituted anthracene and diketopyrrolopyrrole compatible with multiple electron acceptors for high efficiency polymer solar cells. *Polym. Chem.* **2015**, *6*, 4013−4019.

(25) Jiang, X.; Xu, Y.; Wang, X.; Wu, Y.; Feng, G.; Li, C.; Ma, W.; Li, W. Non-fullerene organic solar cells based on diketopyrrolopyrrole polymers as electron donors and ITIC as an electron acceptor. *Phys. Chem. Chem. Phys.* **2017**, *19*, 8069−8075.

(26) Zhao, C.; Guo, Y.; Zhang, Y.; Yan, N.; You, S.; Li, W. Diketopyrrolopyrrole-based conjugated materials for non-fullerene organic solar cells. *J. Mater. Chem. A* **2019**, *7*, 10174−10199.

(27) Song, X.; Gasparini, N.; Nahid, M. M.; Paleti, S. H. K.; Li, C.; Li, W.; Ade, H.; Baran, D. Efficient DPP donor and nonfullerene acceptor organic solar cells with high photon-to-current ratio and low energetic loss. *Adv. Funct. Mater.* **2019**, *29*, 1902441.

(28) Pan, L.; Liu, T.; Wang, J.; Ye, L.; Luo, Z.; Ma, R.; Pang, S.; Chen, Y.; Ade, H.; Yan, H.; et al. Efficient organic ternary solar cells employing narrow band gap diketopyrrolopyrrole polymers and nonfullerene acceptors. *Chem. Mater.* **2020**, *32*, 7309−7317.

(29) Tait, J. G.; Wong, C.; Cheyns, D.; Turbiez, M.; Rand, B. P.; Heremans, P. Ultrasonic spray coating of 6.5% efficient diketopyrro-lopyrrole-based organic photovoltaics. *IEEE J. Photovolt.* **2014**, *4*, 1538−1544.

(30) Bartesaghi, D.; Turbiez, M.; Koster, L. J. A. Charge transport and recombination in PDPP5T:[70]PCBM organic solar cells: The influence of morphology. *Org. Electron.* **2014**, *15*, 3191−3202.

(31) Ji, Y.; Xiao, C.; Wang, Q.; Zhang, J.; Li, C.; Wu, Y.; Wei, Z.; Zhan, X.; Hu, W.; Wang, Z.; et al. Asymmetric diketopyrrolopyrrole conjugated polymers for field-effect transistors and polymer solar cells processed from a non-chlorinated solvent. *Adv. Mater.* **2016**, *28*, 943−950.

(32) Leenaers, P. J.; Wienk, M. M.; Janssen, R. A. J. Structural design of asymmetric diketopyrrolopyrrole polymers for organic solar cells processed from a non-halogenated solvent. *Org. Electron.* **2020**, *86*, 105914.

(33) Cui, Y.; Yao, H.; Hong, L.; Zhang, T.; Tang, Y.; Lin, B.; Xian, K.; Gao, B.; An, C.; Bi, P.; et al. Organic photovoltaic cell with 17% efficiency and superior processability. *Natl. Sci. Rev.* **2020**, *7*, 1239−1246.

(34) Cui, Y.; Yao, H.; Zhang, J.; Zhang, T.; Wang, Y.; Hong, L.; Xian, K.; Xu, B.; Zhang, S.; Peng, J.; et al. Over 16% efficiency organic photovoltaic cells enabled by a chlorinated acceptor with increased open-circuit voltages. *Nat. Commun.* **2019**, *10*, 2515.

(35) Yao, H.; Cui, Y.; Yu, R.; Gao, B.; Zhang, H.; Hou, J. Design, synthesis, and photovoltaic characterization of a small molecular acceptor with an ultra-narrow band gap. *Angew. Chem., Int. Ed.* **2017**, *56*, 3045−3049.

(36) Liu, Y.; Cheng, P.; Li, T.; Wang, R.; Li, Y.; Chang, S.-Y.; Zhu, Y.; Cheng, H.-W.; Wei, K.-H.; Zhan, X.; et al. Unraveling sunlight by transparent organic semiconductors toward photovoltaic and photo-synthesis. *ACS Nano* **2019**, *13*, 1071−1077.

(37) Dueggeli, M.; Zaher Eteish, M.; Hayoz, P.; Aebischer, O. F.; Fonrodona Turon, M.; Turbiez, M. G. R. Diketopyrrolopyrrole polymers for use in organic semiconductor devices. WO 2010049323 A1, 2010.

(38) Willems, R. E. M.; Weijtens, C. H. L.; de Vries, X.; Coehoorn, R.; Janssen, R. A. J. Relating frontier orbital energies from voltammetry and photoelectron spectroscopy to the open-circuit voltage of organic solar cells. *Adv. Energy Mater.* **2019**, *9*, 1803677.

(39) Burkhard, G. F.; Hoke, E. T.; McGehee, M. D. Accounting for interference, scattering, and electrode absorption to make accurate internal quantum efficiency measurements in organic and other thin solar cells. *Adv. Mater.* **2010**, *22*, 3293−3297.

(40) Dyson, M. J.; Van der Pol, T. P. A.; Meskers, S. C. J. Extrinsic influences on photoluminescence spectral lineshape in thin films. *Adv. Opt. Mater.* **2021**, 2001997.

(41) van Franeker, J. J.; Turbiez, M.; Li, W.; Wienk, M. M.; Janssen, R. A. J. A real-time study of the benefits of co-solvents in polymer solar cell processing. *Nat. Commun.* **2015**, *6*, 6229.

(42) Li, C.; Zhang, A.; Feng, G.; Yang, F.; Jiang, X.; Yu, Y.; Xia, D.; Li, W. A systematical investigation of non-fullerene solar cells based on diketopyrrolopyrrole polymers as electron donor. *Org. Electron.* **2016**, *35*, 112−117.

(43) Ye, L.; Jiang, W.; Zhao, W.; Zhang, S.; Cui, Y.; Wang, Z.; Hou, J. Toward efficient non-fullerene polymer solar cells: Selection of donor polymers. *Org. Electron.* **2015**, *17*, 295−303.

(44) Negash, A.; Genene, Z.; Thiruvallur Eachambadi, R.; Kesters, J.; Van den Brande, N.; D'Haen, J.; Penxten, H.; Abdulahi, B. A.; Wang, E.; Vandewal, K.; et al. Diketopyrrolopyrrole-based terpolymers with tunable broad band absorption for fullerene and fullerene-free polymer solar cells. *J. Mater. Chem. C* **2019**, *7*, 3375−3384.

(45) van Franeker, J. J.; Heintges, G. H. L.; Schaefer, C.; Portale, G.; Li, W.; Wienk, M. M.; van der Schoot, P.; Janssen, R. A. J. Polymer solar cells: Solubility controls fiber network formation. *J. Am. Chem. Soc.* **2015**, *137*, 11783−11794.

(46) Murgatroyd, P. N. Theory of space-charge-limited current enhanced by Frenkel effect. *J. Phys. D: Appl. Phys.* **1970**, *3*, 151−156.

(47) Blakesley, J. C.; Castro, F. A.; Kylberg, W.; Dibb, G. F. A.; Arantes, C.; Valaski, R.; Cremona, M.; Kim, J. S.; Kim, J.-S. Towards reliable charge-mobility benchmark measurements for organic semi-conductors. *Org. Electron.* **2014**, *15*, 1263−1272.

(48) Ren, Y.; Hiszpanski, A. M.; Whittaker-Brooks, L.; Loo, Y.-L. Structure−property relationship study of substitution effects on isoindigo-based model compounds as electron donors in organic solar cells. *ACS Appl. Mater. Interfaces* **2014**, *6*, 14533−14542.

(49) Ghosh, S.; Li, X.-Q.; Stepanenko, V.; Würthner, F. Control of H- and J-type π stacking by peripheral alkyl chains and self-sorting phenomena in perylene bisimide homo- and heteroaggregates. *Chem.—Eur. J.* **2008**, *14*, 11343−11357.

(50) Spano, F. C.; Clark, J.; Silva, C.; Friend, R. H. Determining exciton coherence from the photoluminescence spectral line shape in poly(3-hexylthiophene) thin films. *J. Chem. Phys.* **2009**, *130*, 074904.

(51) Spano, F. C.; Silva, C. H- and J-aggregate behavior in polymeric semiconductors. *Annu. Rev. Phys. Chem.* **2014**, *65*, 477−500.

(52) Clark, J.; Silva, C.; Friend, R. H.; Spano, F. C. Role of intermolecular coupling in the photophysics of disordered organic semiconductors: aggregate emission in regioregular polythiophene. *Phys. Rev. Lett.* **2007**, *98*, 206406.

(53) Hestand, N. J.; Spano, F. C. Expanded Theory of H- and J-molecular aggregates: The effects of vibronic coupling and intermolecular charge transfer. *Chem. Rev.* **2018**, *118*, 7069−7163.

(54) Kahle, F.-J.; Saller, C.; Olthof, S.; Li, C.; Lebert, J.; Weiß, S.; Herzig, E. M.; Hüttner, S.; Meerholz, K.; Strohriegl, P.; et al. Does electron delocalization influence charge separation at donor−acceptor interfaces in organic photovoltaic cells? *J. Phys. Chem. C* **2018**, *122*, 21792−21802.

(55) Shen, X.; Han, G.; Yi, Y. The nature of excited states in dipolar donor/fullerene complexes for organic solar cells: evolution with the donor stack size. *Phys. Chem. Chem. Phys.* **2016**, *18*, 15955−15963.

(56) Ran, N. A.; Roland, S.; Love, J. A.; Savikhin, V.; Takacs, C. J.; Fu, Y.-T.; Li, H.; Coropceanu, V.; Liu, X.; Brédas, J.-L.; et al. Impact of interfacial molecular orientation on radiative recombination and charge generation efficiency. *Nat. Commun.* **2017**, *8*, 79.

(57) Chen, H.; Hu, D.; Yang, Q.; Gao, J.; Fu, J.; Yang, K.; He, H.; Chen, S.; Kan, Z.; Duan, T.; et al. All-small-molecule organic solar cells with an ordered liquid crystalline donor. *Joule* **2019**, *3*, 3034−3047.

(58) Zhong, Y.; Causa', M.; Moore, G. J.; Krauspe, P.; Xiao, B.; Günther, F.; Kublitski, J.; Shivhare, R.; Benduhn, J.; BarOr, E.; et al. Sub-picosecond charge-transfer at near-zero driving force in polymer:-non-fullerene acceptor blends and bilayers. *Nat. Commun.* **2020**, *11*, 833.

(59) List, M.; Sarkar, T.; Perkhun, P.; Ackermann, J.; Luo, C.; Würfel, U. Correct determination of charge transfer state energy from luminescence spectra in organic solar cells. *Nat. Commun.* **2018**, *9*, 3631.

(60) Tvingstedt, K.; Vandewal, K.; Gadisa, A.; Zhang, F.; Manca, J.; Inganäs, O. Electroluminescence from charge transfer states in polymer solar cells. *J. Am. Chem. Soc.* **2009**, *131*, 11819−11824.

(61) Kaiser, C.; Zeiske, S.; Meredith, P.; Armin, A. Determining ultralow absorption coefficients of organic semiconductors from the sub-bandgap photovoltaic external quantum efficiency. *Adv. Opt. Mater.* **2020**, *8*, 1901542.

(62) Rau, U. Reciprocity relation between photovoltaic quantum efficiency and electroluminescent emission of solar cells. *Phys. Rev. B: Condens. Matter Mater. Phys.* **2007**, *76*, 085303.

(63) Krückemeier, L.; Rau, U.; Stolterfoht, M.; Kirchartz, T. How to report record open-circuit voltages in lead-halide perovskite solar cells. *Adv. Energy Mater.* **2020**, *10*, 1902573.

(64) Zarrabi, N.; Sandberg, O. J.; Zeiske, S.; Li, W.; Riley, D. B.; Meredith, P.; Armin, A. Charge-generating mid-gap trap states define the thermodynamic limit of organic photovoltaic devices. *Nat. Commun.* **2020**, *11*, 5567.

(65) Song, X.; Gasparini, N.; Ye, L.; Yao, H.; Hou, J.; Ade, H.; Baran, D. Controlling blend morphology for ultrahigh current density in nonfullerene acceptor-based organic solar cells. *ACS Energy Lett.* **2018**, *3*, 669−676.

(66) Zhang, A.; Wang, Q.; Bovee, R. A. A.; Li, C.; Zhang, J.; Zhou, Y.; Wei, Z.; Li, Y.; Janssen, R. A. J.; Wang, Z.; Li, W. Perfluoroalkyl-substituted conjugated polymers as electron acceptors for all-polymer solar cells: the effect of diiodoperfluoroalkane additives. *J. Mater. Chem. A* **2016**, *4*, 7736−7745.

(67) Wehenkel, D. J.; Koster, L. J. A.; Wienk, M. M.; Janssen, R. A. J. Influence of injected charge carriers on photocurrents in polymer solar cells. *Phys. Rev. B: Condens. Matter Mater. Phys.* **2012**, *85*, 125203.

(68) Yang, X.; Loos, J.; Veenstra, S. C.; Verhees, W. J. H.; Wienk, M. M.; Kroon, J. M.; Michels, M. A. J.; Janssen, R. A. J. Nanoscale morphology of high-performance polymer solar cells. *Nano Lett.* **2005**, *5*, 579−583.

(69) Veldman, D.; Meskers, S. C. J.; Janssen, R. A. J. The energy of charge-transfer states in electron donor−acceptor blends: insight into

the energy losses in organic solar cells. *Adv. Funct. Mater.* **2009**, *19*, 1939−1948.

(70) Vandewal, K.; Oosterbaan, W. D.; Bertho, S.; Vrindts, V.; Gadisa, A.; Lutsen, L.; Vanderzande, D.; Manca, J. V. Varying polymer crystallinity in nanofiber poly(3-alkylthiophene): PCBM solar cells: Influence on charge-transfer state energy and open-circuit voltage. *Appl. Phys. Lett.* **2009**, *95*, 123303.

(71) Rosenthal, K. D.; Hughes, M. P.; Luginbuhl, B. R.; Ran, N. A.; Karki, A.; Ko, S. J.; Hu, H.; Wang, M.; Ade, H.; Nguyen, T. Q. Quantifying and understanding voltage losses due to nonradiative recombination in bulk heterojunction organic solar cells with low energetic offsets. *Adv. Energy Mater.* **2019**, *9*, 1901077.

(72) Azzouzi, M.; Yan, J.; Kirchartz, T.; Liu, K.; Wang, J.; Wu, H.; Nelson, J. Nonradiative energy losses in bulk-heterojunction organic photovoltaics. *Phys. Rev. X* **2018**, *8*, 31055.

(73) Koster, L. J. A.; Kemerink, M.; Wienk, M. M.; Maturová, K.; Janssen, R. A. J. Quantifying bimolecular recombination losses in organic bulk heterojunction solar cells. *Adv. Mater.* **2011**, *23*, 1670−1674.

(74) Kim, M.-S.; Kim, B.-G.; Kim, J. Effective variables to control the fill factor of organic photovoltaic cells. *ACS Appl. Mater. Interfaces* **2009**, *1*, 1264−1269.

(75) Huang, B.; Amonoo, J. A.; Li, A.; Chen, X. C.; Green, P. F. Role of domain size and phase purity on charge carrier density, mobility, and recombination in poly(3-hexylthiophene):phenyl-C_{61}-butyric acid methyl ester devices. *J. Phys. Chem. C* **2014**, *118*, 3968−3975.

(76) Venkatesan, S.; Chen, J.; Ngo, E. C.; Dubey, A.; Khatiwada, D.; Zhang, C.; Qiao, Q. Critical role of domain crystallinity, domain purity and domain interface sharpness for reduced bimolecular recombination in polymer solar cells. *Nano Energy* **2015**, *12*, 457−467.

(77) Pan, M. A.; Lau, T. K.; Tang, Y.; Wu, Y.-C.; Liu, T.; Li, K.; Chen, M.-C.; Lu, X.; Ma, W.; Zhan, C. 16.7%-efficiency ternary blended organic photovoltaic cells with PCBM as the acceptor additive to increase the open-circuit voltage and phase purity. *J. Mater. Chem. A* **2019**, *7*, 20713−20722.